Metal–insulator transition characteristics of Mo- and Mn-doped VO_2 films fabricated by magnetron cosputtering technique

2014 Jpn. J. Appl. Phys. 53 063201

(http://iopscience.iop.org/1347-4065/53/6/063201)

Japanese Journal of Applied Physics **53**, 063201 (2014) **REGULAR PAPER**
http://dx.doi.org/10.7567/JJAP.53.063201

Metal–insulator transition characteristics of Mo- and Mn-doped VO_2 films fabricated by magnetron cosputtering technique

Shiu-Jen Liu[1]*, Hau-Wei Fang[2], Yu-Tai Su[3], and Jang-Hsing Hsieh[3]

[1]*Department of Mathematics and Science (Pre-college), National Taiwan Normal University, New Taipei City 244, Taiwan*
[2]*Department of Materials Science and Engineering, National Chiao Tung University, Hsinchu 300, Taiwan*
[3]*Department of Materials Engineering, Mingchi University of Technology, New Taipei City 243, Taiwan*
E-mail: sjliu@ntnu.edu.tw

Received January 10, 2014; accepted March 13, 2014; published online May 21, 2014

Mo- and Mn-doped VO_2 thin films have been grown on *c*-cut sapphire substrates by the magnetron co-sputtering technique. The effects of Mo and Mn doping on the structure and metal–insulator transition of the doped VO_2 thin films were studied. An enlargement of the out-of-plane lattice constant of the film caused by Mo doping was observed. As expected, the transition temperature (T_{MI}) is reduced by Mo doping. However, the valence of the Mo ions doped in the VO_2 films is determined by X-ray photoelectron spectroscopy to be 6+ on the surface, but 4+ and 3+ in the bulk part of the films. The reduction in T_{MI} observed in this study is attributed to the variation in the band structure resulting from the incorporation of Mo^{4+} into the VO_2 lattice. The optical transmission is remarkably enhanced by low-concentration Mo doping and then monotonically decreases with increasing Mo content. On the other hand, the out-of-plane lattice constant and T_{MI} are not affected by Mn doping. The transmission is enhanced and then monotonically increases with increasing Mn concentration. The thermochromism of doped films is suppressed by Mo and Mn doping.

1. Introduction

VO_2 exhibits a metal–insulator (M–I) transition on cooling through a transition temperature (T_{MI}) of about 68 °C.[1)] The M–I transition is accompanied by a first-order crystallographic change from a tetragonal rutile structure ($P4_2/mnm$) (high-temperature state) to a monoclinic structure ($P2_1/c$) (low-temperature state). In the high-temperature state, VO_2 shows metallic conductivity and infrared (IR) reflectivity. In the low-temperature state, VO_2 is an electrical insulator and transparent to IR light. The marked changes in the electrical and optical properties associated with the M–I transition make VO_2 a promising material for a wide variety of applications including temperature sensing devices,[2)] optical filters or switching devices,[3,4)] modulators and polarizers of submillimeter waves,[5)] optical data storage media,[6)] memory materials,[7)] field-effect transistors,[8,9)] noncooled infrared bolometers,[10)] and smart windows.[11,12)] The driving mechanism of the M–I transition is still under debate and has long been argued whether if is the Mott[13)] or Peierls[14)] transition. In the Mott picture, electron correlations predominate the formation of the charge gap in the low-temperature state, while in the Peierls picture, the crystal distortion with the V–V dimerization splits t_{2g} orbitals into e_g^{π} and a_{1g} bands, as suggested by Goodenough.[15)] It has recently been argued that the structural distortion or electron correlation is not solely sufficient to split t_{2g} orbitals and makes VO_2 insulating. Therefore, both mechanisms are suggested to be active for the M–I transition.[16–18)] Moreover, the M–I transition characteristics can be controlled by doping with impurities. Doping VO_2 with large and high-valence cations, such as W^{6+}, Nb^{5+}, and Mo^{6+}, can lower T_{MI}.[19–23)] The reduction in T_{MI} is generally attributed to the loss of V^{4+}–V^{4+} pairs caused by the substitution of V^{4+} with high-valence cations and by the introduction of extra electrons by chemical substitution.[15,24)] The increase in electron concentration has been proposed to play an important role in the reduction in T_{MI}. Nevertheless, for Mo-doped VO_2 with a reduced T_{MI}, there is a discrepancy between the literature values of the valence of Mo ions, e.g., Mo^{4+},[25)] Mo^{5+},[26)] and Mo^{6+}.[27)] In this study, we investigated the valence of Mo ions doped in VO_2 films and the effects of Mo doping on the M–I transition characteristics of doped VO_2 films. For comparison, the effects of Mn doping on the VO_2 films were also explored.

2. Experimental procedure

The undoped, Mo-doped, and Mn-doped VO_2 films used in this study were fabricated on *c*-cut sapphire substrates by magnetron cosputtering. The sputtering was conducted with a 300 W RF power applied to a V_2O_3 target and various DC powers applied to the Mo and Mn targets to control the Mo and Mn concentrations in the films. The substrate temperature was 450 °C. The distance between the target and the substrate was 10 cm. The chamber was evacuated to 1.0×10^{-6} Torr before sputtering, then backfilled to a total gas pressure of 9.0×10^{-3} Torr by introducing a mixture of Ar and O_2 ($O_2/[Ar + O_2]$ [= 1.0–1.2%]). After a 30 min sputtering, the substrate temperature was kept at 450 °C and the films were in-situ-annealed in vacuum (0.8×10^{-6}–1.0×10^{-6} Torr) for 30 min to enhance the crystallinity and eliminate/minimize the V_2O_5 phase, which is generally observed in VO_2 powders and films. After annealing, the films were naturally cooled to room temperature. The Mo and Mn content ratios, i.e., Mo/[V + Mo] and Mn/[V + Mn] (at. %), of the samples were estimated using energy-dispersive X-ray spectrometry and are listed in Table I. The thickness of the films was about 35 nm, as determined from cross-sectional scanning electron microscopy images. The crystal structure of the films was examined from X-ray diffraction (XRD) patterns using the Cu Kα line (PANalytical X'Pert PRO MPD). The V 2p, O 1s, and Mo 2p states of the Mo-doped films were investigated by X-ray photoelectron spectroscopy (XPS) using the Thermo VG Scientific ESCALAB 250 system with an Al Kα X-ray source (1486.6 eV). The analysis chamber was equipped with a flood gun used for charge compensation when necessary. The XPS profiles were referenced to the C 1s photoemission line of 284.5 eV. The van der Pauw configuration was employed to measure the room-temperature resistivity. The temperature-dependent resistivities of all the films were determined to

Table I. P_{Mo} and P_{Mn} are the DC powers applied to the Mo and Mn targets, respectively. Mo and Mn are the Mo/[V + Mo] and Mn/[V + Mn] content ratios, respectively.

	Mo#1	Mo#2	Mo#3	Mo#4
P_{Mo} (W)	5	7	10	12
Mo (at.%)	3.7	6.9	12.2	15.5
	Mn#1	Mn#2	Mn#3	Mn#4
P_{Mn} (W)	3	5	7	10
Mn (at.%)	1.4	4.0	8.3	12.4

investigate the M–I transition characteristics. Optical transmission was recorded at 25 and 95 °C using a UV–visible spectrophotometer.

3. Results and discussion

The θ–2θ XRD scans were taken between $2\theta = 20$ and 80° for all the films at room temperature. Except for the peaks contributed by the substrates, only a peak centered at $2\theta =$ 39.93–39.53° was observed for each film, indicating the textured structure of the prepared films. The XRD patterns ($2\theta = 35$–45°) of the Mo- and Mn-doped films are shown in Figs. 1(a) and 1(b), respectively. The XRD pattern of the undoped VO_2 film is also shown in Fig. 1(b) for comparison. The peak centered at $2\theta \sim 39.9°$ for the VO_2 films grown on *c*-cut sapphires is generally assigned to the (020) or (002) diffraction (JCPDS Card No. 82-0661). Because of their nearly identical *d*-spacings, it is difficult to distinguish between (00*l*) and (0*l*0) peaks of VO_2.[28] Furthermore, as seen in Fig. 1(a), the shift of the XRD peak of the Mo-doped films toward low 2θ values with increasing Mo content ratio reveals an increase in the out-of-plane *d*-spacing, which is undoubtedly a result of the substitution of V with Mo in the VO_2 lattice. It also indicates a larger radius of the Mo ions than that of the V ions in the doped films. On the other hand, as shown in Fig. 1(b), the 2θ values of the XRD peaks observed in the Mn-doped VO_2 films are the same as those of the undoped VO_2 films. This reveals the similarity between the ionic radii of the Mn and V ions in the Mn-doped VO_2 films. Moreover, for the Mo-doped films, the intensity of the XRD peaks increases with increasing Mo content ratio, indicating an improvement in the crystallinity of the films. In contrast, the intensity of the XRD peaks of the Mn-doped films decreases with increasing Mn content ratio. For samples Mn#3 and Mn#4, the low intensities of the XRD peaks indicate the poor crystallinity of the VO_2 films doped with a high concentration of Mn.

It is well known that the M–I transition characteristics of doped VO_2 films strongly depend on the valence states of V and the dopant. V 2p, O 1s, and Mo 3d core-level XPS measurements were carried out at room temperature to determine the valence states of the elements in the Mo-doped films. Figures 2(a)–2(c) respectively show the V 2p, O 1s, and Mo 3d XPS profiles measured from the surfaces of the undoped and Mo-doped VO_2 films. As shown in Fig. 2(a), two maxima were observed in the V 2p XPS profiles of each sample. The maxima at low binding energies (516.8 and 518.1 eV) were fitted by two Gaussian peaks (VO_2 is taken as an example). These two peaks are labeled V^{4+} and V^{5+} according to their positions and can be assigned

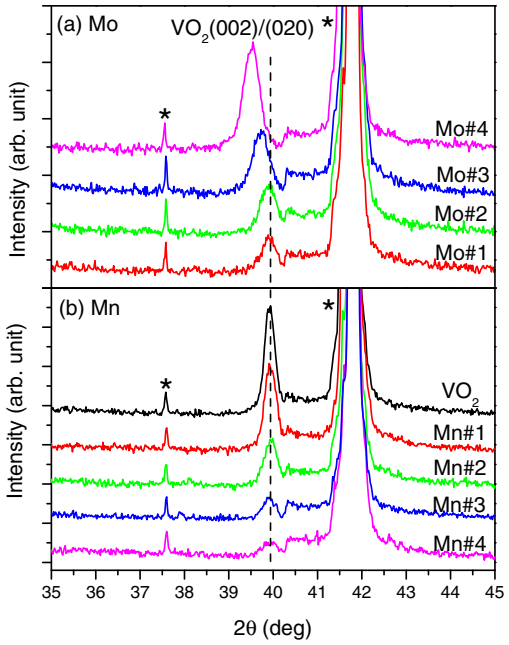

Fig. 1. (Color online) XRD patterns of (a) Mo- and (b) Mn-doped VO_2 films. The XRD curve for undoped VO_2 film (denoted as VO_2) is plotted in (b) for comparison. The Mo and Mn content ratios are listed in Table I. The asterisks denote the diffraction peaks of the sapphire substrates.

to $2p_{3/2}$ lines of V^{4+} and V^{5+}, respectively.[29] The V^{5+} peaks indicate the presence of V^{5+} ions, i.e., V_2O_5 phases that produced by overoxidation. The V_2O_5 phase is also observed on the surface of commercial VO_2 and V_2O_3 powders,[29,30] and attributed to air oxidation. Moreover, the increase in the area of V^{5+} peaks in Mo-doped VO_2 films indicates the enhancement of overoxidation on the film surface by Mo doping. Note that, in contrast, Zhang et al.[31] and Cui and Ramanathan[32] reported the enhanced oxidation durability in VO_2 films grown on TiO_2-buffered fused quartz and single-crystalline TiO_2 substrates. It was ascribed to the epitaxial growth of VO_2 films and Ti diffusion into the VO_2 crystals. The enhanced overoxidation by Mo doping observed here possibly results from the tensile strain caused by the chemical substitution. The maxima at high binding energies (524.5 and 525.2 eV) are assigned to the V $2p_{1/2}$ core levels. Moreover, as seen in the figure, the V $2p_{1/2}$ peaks in Mo-doped films shift to high binding energies. Since the binding energy of V^{5+} $2p_{1/2}$ is higher than that of V^{4+} $2p_{1/2}$,[30] the shift of V $2p_{1/2}$ lines results from the variation in the valence states of the V ions in the Mo-doped VO_2 films. Figure 2(b) shows the O 1s XPS profiles that can be fitted by combining two Gaussian peaks (VO_2 is taken as an example). The fitting peaks with low binding energies (~530.5 eV) are referred to as the low-binding-energy component (LBEC) and have been ascribed to the O 1s core peak of O^{2-} bound to V ions.[33] The peaks centered at 531.5–531.8 eV are the high-binding-energy components (HBECs), which have been suggested to be directly related to hydroxides, organic oxygen, or oxygen vacancies.[33] Figure 2(c) shows the Mo 3d XPS profiles. The two peaks located at 235.5 and 232.3 eV can be assigned to Mo^{6+} $3d_{3/2}$ and $3d_{5/2}$, respectively.[34] The Mo dopants are fully oxidized to be Mo^{6+}.

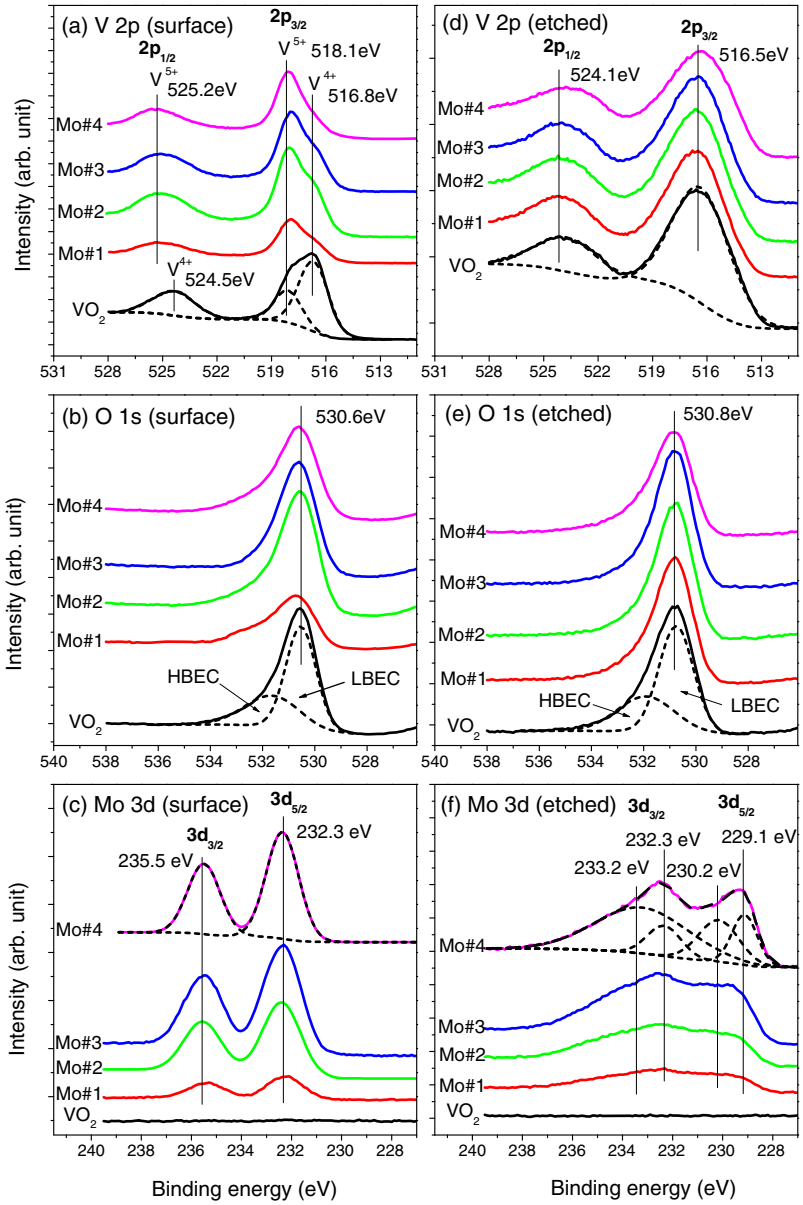

Fig. 2. (Color online) (a–c) are respectively the V 2p, O 1s, and Mo 3d XPS profiles measured from the surface of the undoped and Mo-doped VO_2 films. (d–f) are respectively the V 2p, O 1s, and Mo 3d XPS profiles measured from the etched films. The dashed lines are Gaussian fitting results with the Shirley background applied.

Note that, for V $2p_{3/2}$ in the Mo-doped VO_2 films, the intensity and area of the V^{5+} peaks are larger than those of the V^{4+} peaks. This indicates that the V_2O_5 phase is the major component in these films. However, since XPS is a surface-sensitive technique and the XRD scans reveal the VO_2 structure for all the samples, the V_2O_5 phase is deduced to exist only on the film surface. Since the surfaces of the films are covered with V_2O_5, in order to elucidate the valence state of elements in the bulk part of the films, XPS was carried out again after the films were etched in the XPS chamber for 30 s. The etching procedure resulted in the removal of a 3-nm-thick surface layer of VO_2 films. The V 2p, O 1s, and Mo 3d XPS profiles measured from the etched films are shown in Figs. 2(d)–2(f), respectively. As shown in Fig. 2(d), the V $2p_{1/2}$ and V $2p_{3/2}$ peaks can be respectively fitted by Gaussian curves centered at binding energies of 524.1 and 516.5 eV, and contributed by V^{4+} ions. This result further confirms that the V_2O_5 phase was formed only on the surfaces of the films. The O 1s XPS profiles of the etched films are plotted in Fig. 2(e). The similarity between Figs. 2(b) and 2(e) indicates that the HBEC component of the O 1s curves shown in Fig. 2(b) is not due to organic contamination. On the other hand, the Mo 3d spectra obtained from the etched films, shown in Fig. 2(f), are quite different from those obtained from the film surface [Fig. 2(c)]. First, the overall spectra obtained from the etched films shift toward low binding energies. Moreover, four Gaussian peaks are needed to deconvolute the XPS curves well. The peaks centered at 233.2 and 230.2 eV were assigned to the $3d_{3/2}$ and $3d_{5/2}$ lines of Mo^{4+} ions, respectively.[35,36] On the other hand, the peaks centered at 232.3 and 229.1 eV were attributed to the $3d_{3/2}$ and $3d_{5/2}$ lines of Mo^{3+} ions, respectively.[36] The existence of Mo^{3+} ions in the films possibly results from the low-O_2-partial-pressure working gas during sputtering or in situ annealing in vacuum after sputtering. For a coordination number of 6, the ionic radii of Mo^{4+} and Mo^{3+} are respectively 0.65 and 0.69 Å, which are

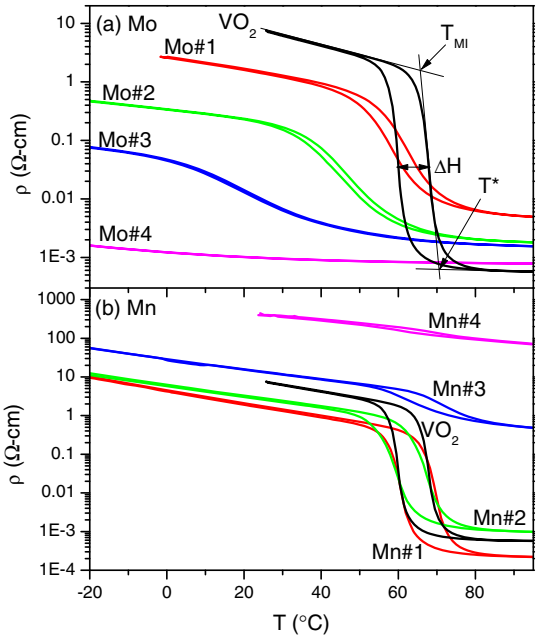

Fig. 3. (Color online) Temperature dependent resistivities [$\rho(T)$] of (a) Mo- and (b) Mn-doped VO_2 films. The transition temperatures T_{MI}, hysteresis widths ΔH and the transition sharpnesses $\Delta T = T^* - T_{MI}$ estimated from the $\rho(T)$ curves for all the films are listed in Table II. The $\rho(T)$ curve for the undoped VO_2 film is plotted in both (a) and (b) for comparison.

larger than that of V^{4+} (0.58 Å).[37] The substitution of V^{4+} with Mo^{4+} or Mo^{3+} is expected to result in an increase in the lattice constants, as revealed by the XRD results.

The temperature-dependent resistivity $\rho(T)$ curves for Mo-doped VO_2 films are shown in Fig. 3(a). As expected, T_{MI} and the resistivity in the insulating states are reduced by Mo doping. However, Hanlon et al.[21] reported enhanced conductivities in both the low-temperature insulating and high-temperature metallic states of VO_2 films by Mo doping and attributed it to the increase in carrier concentration caused by the introduction of the expected Mo^{6+} ions, similarly to that observed in oxygen-deficient VO_2 films.[38] In this study, although the resistivity of the Mo-doped films was monotonically decreased by increasing the Mo doping level, the resistivity in the metallic state is higher than that of the undoped VO_2 film, i.e., Mo doping increases the resistivity of VO_2 films in the metallic state. Moreover, the XRD and XPS results indicate the valences of the Mo ions in our Mo-doped VO_2 films are 4+ and 3+, not 6+. The reduction in T_{MI} observed in Mo-doped films can not be ascribed to the introduction of extra electrons by chemical substitution. It was also reported that the compressive strain along the *c*-axis of VO_2 films decreases T_{MI}, whereas the tensile strain along the same axis increase T_{MI}.[39] Owing to the substitution of V ions with larger Mo^{4+} and Mo^{3+} in our Mo-doped films, the expansion in the *c*-axis lattice constant is expected. Therefore, the reduced T_{MI} observed here cannot be explained by the compressive strain along the *c*-axis. Furthermore, the T_{MI}s of samples Mo#3 and Mo#4 are below room temperature, at which both samples have a monoclinic structure, i.e., the M–I transitions of these two heavily doped samples are not related to a crystallographic change. It is worth noting that MoO_2 is metallic and isostructural to monoclinic VO_2 at room temperature. The decreases in both low-temperature resistivity and T_{MI} with Mo doping could be attributed to the variation in the band structure resulting from the incorporation of Mo^{4+} ions in the VO_2 lattice. The thermal hysteresis width ΔH, which is associated with the microstructure of films,[40,41] is systematically narrowed by Mo doping. The $\rho(T)$ curves for the Mn-doped VO_2 films are plotted in Fig. 3(b). Although the T_{MI}s of samples Mn#2–#4 are lower than that of the undoped VO_2 film, they do not monotonically decrease with increasing Mn doping level. Although the low- and high-temperature resistivities of sample Mn#1 are lower than those of undoped VO_2, the resistivities of Mn-doped samples increased with Mn doping, which could be ascribed to defect scattering and poor crystallinity. To compare the M–I transition characteristics of the undoped and doped films, parameters including T_{MI}, transition sharpness (ΔT), thermal hysteresis width (ΔH), and the change in electrical resistivity $R = \rho(25C)/\rho(95C)$ are determined from the $\rho(T)$ curves and listed in Table II. T_{MI} is determined by the intersection of the extrapolation lines of the $\rho(T)$ curves in the insulating and transition regimes, as depicted in Fig. 3(a). Moreover, $\Delta T = T^* - T_{MI}$, where T^* is determined by the intersection of the extrapolation lines of the $\rho(T)$ curves in the metallic and transition regimes. ΔH is the thermal hysteresis width at the temperature $(T_{MI} + T^*)/2$. $\rho(25C)$ and $\rho(95C)$ are the resistivities measured at 25 and 95 °C, respectively.

Table II. M–I transition characteristics including T_{MI}, $\Delta T = T^* - T_{MI}$, ΔH and the change in resistivity $R = \rho(25C)/\rho(95C)$ of all the samples. The definitions of T^*, T_{MI}, ΔH, $\rho(25C)$, and $\rho(95C)$ are shown in Fig. 3 and explained in the text.

Sample	T_{MI} (°C)	ΔT (°C)	ΔH (°C)	R
VO_2	65.7	4.4	7.7	13232
Mo#1	53.0	18.8	3.8	298
Mo#2	34.3	27.6	2.3	119
Mo#3	2.9	44.0	1.6	6.0
Mo#4	−91.1	107	0	1.2
Mn#1	66.3	6.9	8.7	7829
Mn#2	62.8	9.5	7.7	2854
Mn#3	64.4	17.6	6.6	27.7
Mn#4	61.1	17.9	6.6	5.57

The optical transmission spectra of the Mo-doped sample measured at 25 °C (in the insulating regime) and 95 °C (in the metallic regime) are shown in Fig. 4(a). First, in comparison with that of undoped VO_2, the transmission is markedly increased by low-concentration Mo doping (sample Mo#1) and then monotonically decreases with increasing Mo content. In contrast, as shown in Fig. 4(b), the transmission of the Mn-doped sample monotonically increases with increasing Mn concentration. The transmission of the doped films is found to correlate with the electrical resistivity. Furthermore, the transmission of all the samples was increased in the range of 500–900 nm by raising the temperature from 25 to 95 °C, i.e., by warming through the M–I transition. Since the thickness of the films used in this study is about 35 nm, this result is consistent with the report by Xu et al.,[42] who demonstrated that, in the range of 500–900 nm, the transmission of VO_2 films with thicknesses below 50 nm in the insulating state below T_{MI} is lower than that in the metallic state above T_{MI}, while the result for VO_2 films with thick-

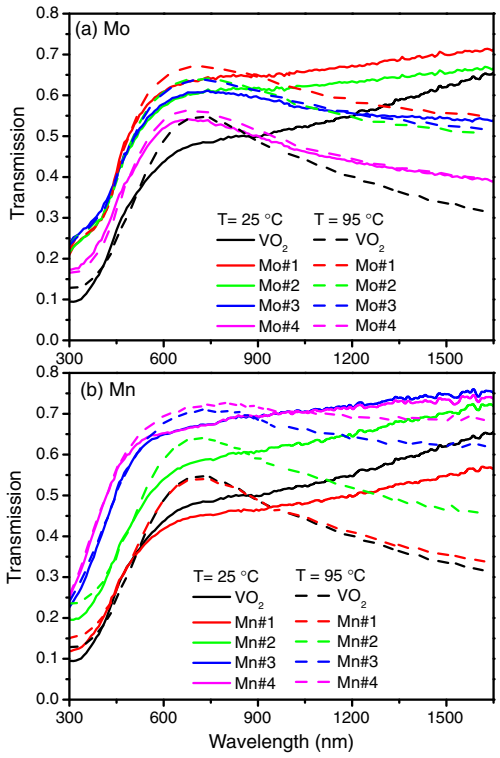

Fig. 4. (Color online) Optical transmission spectra of (a) Mo- and (b) Mn-doped VO_2 films measured at 25 °C (solid lines) and 95 °C (dashed lines), respectively. The spectrum of the undoped VO_2 film is plotted in both (a) and (b) for comparison.

nesses above 50 nm is reverse. As expected, owing to the M–I transition, the transmission of the undoped VO_2 film in the near-IR region is strongly suppressed, while the temperature is raised from 25 to 95 °C. However, for the Mo- and Mo-doped samples, the difference between the IR transmissions measured at 25 and 95 °C, i.e., thermochromism is gradually suppressed by increasing the dopant concentration.

4. Conclusions

In this study, textured Mo- and Mn-doped VO_2 films were fabricated on *c*-cut sapphire substrates by RF magnetron cosputtering. The XPS and XRD measurements indicated that the valence of the Mo ions on the surface of doped VO_2 films was 6+, but 4+ and 3+ in the bulk part of Mo-doped films. The reductions in the low-temperature resistivity and T_{MI} of Mo-doped films were attributed to the variation in the band structure caused by the incorporation of Mo^{4+} into the VO_2 lattice. On the other hand, the T_{MI} of the Mn-doped VO_2 films was slightly affected by the Mn doping. The transmission of doped films was decreased and increased with increasing Mo and Mn concentrations, respectively. The thermochromism of the doped films was suppressed by Mo and Mn doping.

Acknowledgement

This work was supported by the National Science Council of Taiwan, R.O.C. under Grant No. NSC 101-2112-M-003-007.

1) F. J. Morin, Phys. Rev. Lett. **3**, 34 (1959).
2) D. C. Yin, N. K. Xu, and J. Y. Zhang, Mater. Res. Bull. **31**, 335 (1996).
3) F. Béteille, L. Mazerolles, and J. Livage, Mater. Res. Bull. **34**, 2177 (1999).
4) J. Livage, Coord. Chem. Rev. **190–192**, 391 (1999).
5) M. A. Richardson and J. A. Coath, Opt. Laser Technol. **30**, 137 (1998).
6) R. T. Kivaisi and M. Samiji, Sol. Energy Mater. Sol. Cells **57**, 141 (1999).
7) T. Driscoll, H. T. Kim, B. G. Chae, B. J. Kim, Y. W. Lee, N. M. Jokerst, S. Palit, D. R. Smith, M. D. Ventra, and D. N. Basov, Science **325**, 1518 (2009).
8) S. Sengupta, K. Wang, K. Liu, A. K. Bhat, S. Dhara, J. Wu, and M. M. Deshmukh, Appl. Phys. Lett. **99**, 062114 (2011).
9) M. Nakano, K. Shibuya, D. Okuyama, T. Hatano, S. Ono, M. Kawasaki, Y. Iwasa, and Y. Tokura, Nature **487**, 459 (2012).
10) H. Jerominek, F. Picard, N. R. Swart, M. Renaud, and M. Levesque, Proc. SPIE **2746**, 60 (1996).
11) T. Ivanova, A. Harizanova, M. Surtchev, and Z. Nenova, Sol. Energy Mater. Sol. Cells **76**, 591 (2003).
12) C. G. Granqvist, Sol. Energy Mater. Sol. Cells **91**, 1529 (2007).
13) T. M. Rice, H. Launois, and L. P. Pouget, Phys. Rev. Lett. **73**, 3042 (1994).
14) R. M. Wentzcovitch, W. W. Schulz, and P. B. Allen, Phys. Rev. Lett. **72**, 3389 (1994).
15) J. B. Goodenough, J. Solid State Chem. **3**, 490 (1971).
16) S. Biermann, A. Poteryaev, A. I. Lichtenstein, and A. Georges, Phys. Rev. Lett. **94**, 026404 (2005).
17) T. C. Koethe, M. W. Haverkort, C. Schusler-Langeheine, F. Venturini, N. B. Brookes, O. Tjernberg, W. Reichelt, H. H. Hsieh, H. J. Lin, C. T. Chen, and L. H. Theng, Phys. Rev. Lett. **97**, 116402 (2006).
18) J. M. Tomczak, F. Aryasetiawan, and S. Biermann, Phys. Rev. B **78**, 115103 (2008).
19) P. Jin and S. Tanemura, Thin Solid Films **281–282**, 239 (1996).
20) Z. P. Wu, A. Miyashita, S. Yamamoto, H. Abe, I. Nashiyama, K. Narumi, and H. Naramoto, J. Appl. Phys. **86**, 5311 (1999).
21) T. J. Hanlon, J. A. Coath, and M. A. Richardson, Thin Solid Films **436**, 269 (2003).
22) K. Shibuya, M. Kawasaki, and Y. Tokura, Appl. Phys. Lett. **96**, 022102 (2010).
23) H. Takami, K. Kawatani, T. Kanki, and H. Tanaka, Jpn. J. Appl. Phys. **50**, 055804 (2011).
24) C. Tang, P. Georggopoulos, M. E. Fine, J. B. Cohen, M. Nygren, G. S. Knapp, and A. Aldred, Phys. Rev. B **31**, 1000 (1985).
25) T. D. Manning, I. P. Parkin, C. Blackman, and U. Qureshi, J. Mater. Chem. **15**, 4560 (2005).
26) C. J. Patridge, L. Whittaker, B. Ravel, and S. Banerjee, J. Phys. Chem. C **116**, 3728 (2012).
27) S. Q. Xu, H. P. Ma, S. X. Dai, and Z. H. Jiang, J. Mater. Sci. **39**, 489 (2004).
28) H. Zhou, M. F. Chisholm, T. H. Yang, S. J. Pennycook, and J. Narayan, J. Appl. Phys. **110**, 073515 (2011).
29) G. Silversmit, D. Depla, H. Poelman, G. B. Marin, and R. De Gryse, J. Electron Spectrosc. Relat. Phenom. **135**, 167 (2004).
30) E. Hryha, E. Rutqvist, and L. Nyborg, Surf. Interface Anal. **44**, 1022 (2012).
31) Z. T. Zhang, Y. F. Gao, L. T. Kang, J. Du, and H. J. Luo, J. Phys. Chem. C **114**, 22214 (2010).
32) Y. Cui and S. Ramanathan, J. Vac. Sci. Technol. A **29**, 041502 (2011).
33) M. C. Biesinger, L. W. M. Lau, A. R. Gerson, and R. St. C. Smart, Appl. Surf. Sci. **257**, 887 (2010).
34) C. D. Wagner, W. M. Riggs, L. E. Davis, J. F. Moulder, and G. E. Muilenberg, *Handbook of X-ray Photoelectron Spectroscopy* (Perkin-Elmer, Eden Prairie, MN, 1979) p. 104.
35) J. G. Choi and L. T. Thompson, Appl. Surf. Sci. **93**, 143 (1996).
36) R. B. Quincy, M. Houalla, A. Proctor, and D. M. Hercules, J. Phys. Chem. **94**, 1520 (1990).
37) R. D. Shannon, Acta Crystallogr., Sect. A **32**, 751 (1976).
38) S. J. Liu, Y. T. Su, and J. H. Hsieh, Jpn. J. Appl. Phys. **53**, 033201 (2014).
39) Y. Muraoka and Z. Hiroi, Appl. Phys. Lett. **80**, 583 (2002).
40) R. Lopez, L. A. Boatner, T. E. Haynes, R. F. Haglund, Jr., and L. C. Feldman, Appl. Phys. Lett. **79**, 3161 (2001).
41) X. F. Xu, X. F. He, H. Y. Wang, Q. J. Gu, S. X. Shi, H. Z. Xing, C. R. Wang, J. Zhang, X. S. Chen, and J. H. Chu, Appl. Surf. Sci. **261**, 83 (2012).
42) G. Xu, P. Jin, M. Tazawa, and K. Yoshmura, Jpn. J. Appl. Phys. **43**, 186 (2004).